SCIENTIFIC REPORTS

OPEN

$BiVO_4$-rGO with a novel structure on steel fabric used as high-performance photocatalysts

Received: 28 February 2017
Accepted: 28 June 2017
Published online: 11 August 2017

Dong Fang[1], Xiujuan Li[1], Hui Liu[2], Weilin Xu[1], Ming Jiang[1], Wenbin Li[1] & Xin Fan[3]

A high-performance and novel photocatalyst of $BiVO_4$-reduced Graphene Oxide ($BiVO_4$-rGO) nanocomposite was prepared by a facile hydrothermal method. The photocatalyst was characterized by X-ray diffraction, X-ray photoelectron spectroscopy, scanning electron microscopy, transmission electronic microscopy, UV-Vis diffusion reflectance spectroscopy, photoluminescence spectroscopy and UV-Vis adsorption spectroscopy, respectively. The visible-light photocatalytic activity was evaluated by oxidation of methyl orange (MO) under simulated sunlight irradiation. The results show that the $BiVO_4$-rGO nanocomposites exhibit enhanced photocatalytic performance for the degradation of MO with a maximum removal rate of 98.95% under visible light irradiation as compared with pure $BiVO_4$ (57.55%) due to the increased light absorption intensity and the degradation of electron-hole pair recombination in $BiVO_4$ with the introduction of the rGO.

Due to the rapid urbanization and industrialization, water pollutions has received increased attention, which presents a challenge to environmental governance[1]. Many methods are available for removing organic dyes from wastewater, including physical-[2], biological-[3], electrochemical-[4], and oxidation- technology[5]. Among them, the advanced oxidation technology, especially the photocatalysis method, has become one of the most important techniques for the degradation of organic contaminants in wastewater[6–13].

Monoclinic bismuth vanadate ($BiVO_4$) has been widely used as a photocalalyst dye treatment under visible light irradiation[14]. The advantages of the compound include a narrow band gap for visible light absorption, abundant availability, low cost and good stability[15]. It is known that the photocatalytic properties of the material greatly depend on its the structure and morphology[16–18]. There are three main crystal structures for $BiVO_4$: monoclinic scheelite, tetragonal zircon, and tetragonal scheelite[19]. Among them, the monoclinic $BiVO_4$ is an n-type semiconductor with a narrow band gap of about 2.4 eV and it has an excellent photocatalytic activity in the visible range for the degradation of organic pollutants because of its appropriate band gap for solar energy conversion[20]. However, the low photocatalytic activity of pure $BiVO_4$ has limited its further use in practical applications due to its poor adsorptive performance and migration difficulty of photo-generated electron-hole pairs[21,22]. To overcome this problem, many efforts have been made to enhance the activity of $BiVO_4$-based photocatalysts. Element dopants added to $BiVO_4$ to increase the donor density and carrier mobility[23] and $BiVO_4$-based composites including homo/hetero-junction construction and co-catalyst loading metal oxide compounds have been investigated[24–27]. These results have shown that the $BiVO_4$-based composites favor the separation of photo-induced electron-hole pairs and result in enhanced photocatalytic activity in the visible range[28].

Recently, two-dimensional (2-D) graphene has increasingly attracted attention due to its fascinating physical properties including quantum electronic transport, extremely high mobility, high elasticity, and electromechanical modulation[29,30]. Graphene oxide has a similar structure as grapheme and the only difference is that the surface and edges of the tgraphene oxide carbon skeleton are modified by oxygen-containing groups[31] (such as -CO-, -OH-, -COOH, C-O-C). There are experiment interactions between the oxygenic functional groups of graphene oxide and different materials by a non-covalent bond, a covalent bond, or an ionic interaction mode, which can easily result in functionalized mixtures and composites with extraordinary properties easily. In recent years,

[1]Key Lab of Green Processing and Functional Textiles of New Textile Materials Ministry of Education, College of Material Science and Engineering, Wuhan Textile University, Wuhan, 410000, P. R. China. [2]School of Metallurgy and Environment, Central South University, Changsha, 410083, P. R. China. [3]College of Materials Science and Engineering, Guilin University of Technology, Guilin, 541004, P. R. China. Correspondence and requests for materials should be addressed to D.F. (email: csufangdong@gmail.com) or M.J. (email: mjiang@wtu.edu.cn) or W.L. (email: Li780713@hotmail.com)

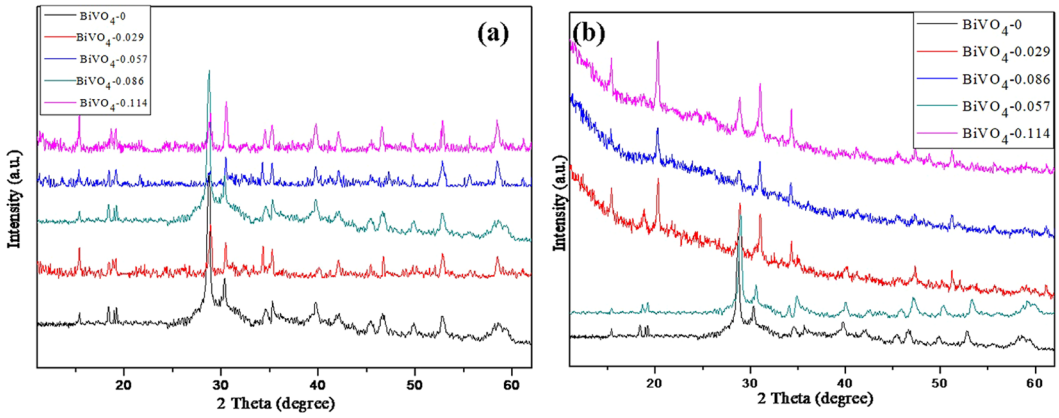

Figure 1. (**a**) XRD patterns of pristine $BiVO_4$ and the $BiVO_4$-rGO nanocomposites, (**b**) Raman spectra of the $BiVO_4$, $BiVO_4$-0.057 composite, and pure graphene oxide.

graphene-based nano-materials have been utilized as photocatalysts to enhance the photocatalytic efficiencies because the such a supporting matrix with excellent electric conductivity and a super-high surface area make excellent contact with water or target pollutants to provide plenty of reactive sites[32–37].

In this work, we present a simple hydrothermal method to prepare $BiVO_4$-rGO composites using graphene oxide (GO) and $Bi(NO_3)_3.5H_2O$ as starting materials. The synthesis processes of $BiVO_4$ nanowires and $BiVO_4$-rGO nanosheets are presented in detail. The photocatalytic activities of $BiVO_4$ and $BiVO_4$-rGO are evaluated for the degradation of MO. The results indicate a superior photocatalytic performance of the $BiVO_4$-rGO composite under simulated sunlight conditions.

Results and Discussion

The crystallographic structure and phase purity of the as-obtained samples are first examined by powder X-ray diffraction (XRD) analysis (Fig. 1a). All the diffraction peaks can be indexed as the body-centered monoclinic phase of $BiVO_4$ with lattice constants of $a = 5.195$ Å, $b = 11.70$ Å and $c = 5.092$ Å (JCPDS card no. 14-0688)[38–40]. The XRD patterns are similar for the $BiVO_4$- rGO composites and the $BiVO_4$. An increase in the content of GO results in no obvious changes in the XRD patterns of the samples, suggesting that the introduction of GO has little influence on the crystalline structure of $BiVO_4$. The Raman spectra at room temperature under green laser excitation (532 nm) are shown in Fig. 1(b). The main Raman peaks of monoclinic $BiVO_4$ are observed around 210, 325, 366, 707 and 827 cm^{-1}, which are consistent with typical vibrational bands of monoclinic $BiVO_4$[41,42]. The dominating peak at 827 cm^{-1} and the inconspicuous peak at 707 cm^{-1} are assigned to the symmetric and antisymmetric V-O stretching mode, respectively. The Peak centered at 366 and 325 cm^{-1} is attributed to the typical symmetric and antisymmetric bending modes of the vanadate anion, respectively. The GO exhibits Raman shifts at 1591 and 1355 cm^{-1}, corresponding to the G- and D-bands, respectively. As for the $BiVO_4$-0.057 nanocomposites, aside from the distinctive peaks assigned to $BiVO_4$, the G- and D-bands of rGO are located at 1588 and 1350 cm^{-1}, respectively, indicating shifts toward lower wavenumbers as compared to GO[43,44].

Figure 2 present typical scanning electron microscopy (SEM) and transmission electron microscopy (TEM) images of the $BiVO_4$ and $BiVO_4$-0.057 products. As shown in Fig. 2a, it can be seen that the as-synthesized $BiVO_4$ has a nanowire structure. The TEM image presented in Fig. 2b reveals that the diameter of $BiVO_4$ is about 66 nm and that the interplanar distance of the (121) plane of the monoclinic $BiVO_4$ is 0.31 nm (Fig. 2c)[45]. Interestingly, after $BiVO_4$ was coupled with rGO, the morphology of the nanowires disappeared completely and sheets-like structures appeared, as shown in Fig. 2d. In the TEM images (Fig. 2e–g), there is a central $BiVO_4$ nanowire axis, which is covered by $BiVO_4$/rGO nanosheets. The thickness of the nanosheets is about 10 nm. The functional groups such as hydroxyl, carboxyl, and carbonyl groups of the GO may provide the reaction sites for the nucleation and growth of the $BiVO_4$-0.057 nanosheets[46]. In the TEM-EDS image of the $BiVO_4$-0.057 nanosheets is tested and presented (Fig. 2h), from which Bi, V, O and C signals are clearly observed.

For a comparison, the morphological structures of the $BiVO_4$-rGO nanocomposites with different synthesis conditions are characterized by the SEM technique(Fig. 3). When the concentration of GO is 0.029 gL^{-1}, the images show that part of the nanowires are covered by nanosheets (Fig. 3(a)). When the GO amount is increased to 0.057 gL^{-1} (Fig. 2c), the nanowires disappear completely and 500-nm wide exhibit nanosheet structures are formed. With a further increase in the GO to 0.086 gL^{-1} (Fig. 3(b)), the nanosheet structure morphology is retained. Figure 3(c) presents the formation diagram of the $BiVO_4$ nanowires and the $BiVO_4$-rGO nanosheets process. Initially, the nanowire-like $BiVO_4$ is obtained on a Ti fabric under hydrothermal condition. When the rGO is incorporated, a portion of the nanowires are covered by nanosheets. As the rGO amount is further increased, more nanosheets are formed on the nanowires. In the detailed structure of the nanosheets, the rGO nanosheets are covered by $BiVO_4$, i.e., a sandwich structure is formed with rGO in the central part.

The surface chemical composition and the chemical states of $BiVO_4$ and $BiVO_4$-0.057 were analyzed by X-ray photoelectron spectroscopy(XPS) (Fig. 4a). Seven obvious peaks corresponding to Bi5d, Bi4f, C1s, $Bi4d^{5/2}$, $Bi4d^{3/2}$, O1s and $V2p^{3/2}$ are detected in both samples. Figure 4b–d shows the XPS spectrum of Bi(b),V(c) and C(d) in the $BiVO_4$-0.057 composite, respectively. XPS signals of Bi 4 f with binding energies at 164.5 eV (Bi $4f^{7/2}$)

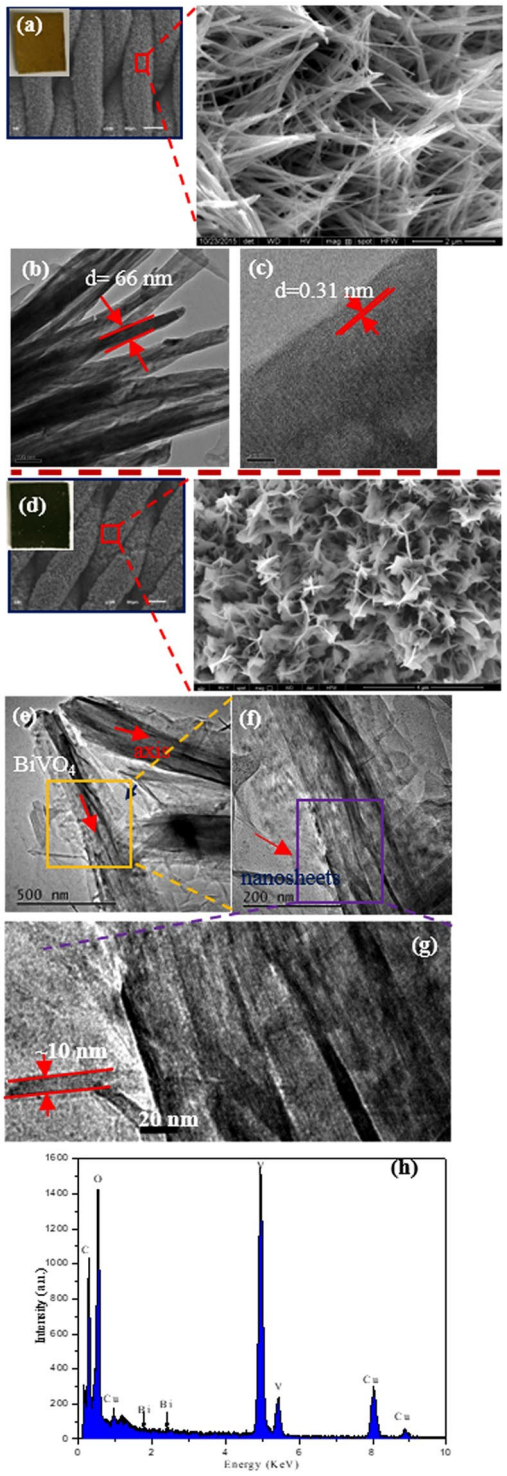

Figure 2. (**a**) SEM, (**B**) and (**C**) low- and high-magnification TEM images of the pure $BiVO_4$, (**d**) SEM, (**e**) and (**f**) low- and high-magnification TEM images of the $BiVO_4$-0.057 nanocomposites. Inset in (**a**) and (**d**) is the corresponding digital picture of sample, (**h**) EDS spectrum of $BiVO_4$-0.057 nanocomposite.

and 159.2 eV (Bi $4f^{5/2}$) are detected (Fig. 4b), which confirm that the Bi species exist as Bi^{3+}[47–51]. The signal of V $2p^{1/2}$ and V $2p^{3/2}$ is located at 524.8 and 516.8 eV, respectively (Fig. 4c), indicating that the V species are in the state of V^{5+}[52,53]. Thus, the electron couples of Bi^{3+} and V^{5+} coexist in the orthorhombic $BiVO_4$ structures, where the total atomic ratio of the Bi and V elements is about 1:1, corresponding to the molecular formula of $BiVO_4$. In the high resolution spectrum of C 1 s (Fig. 4d), carbons in the form of sp^2 bonds (284.6 eV) are dominated and oxygen-containing functional group is also observed at 288.6 eV (C = O), which may represent the absorption of atmospheric CO_2[54,55].

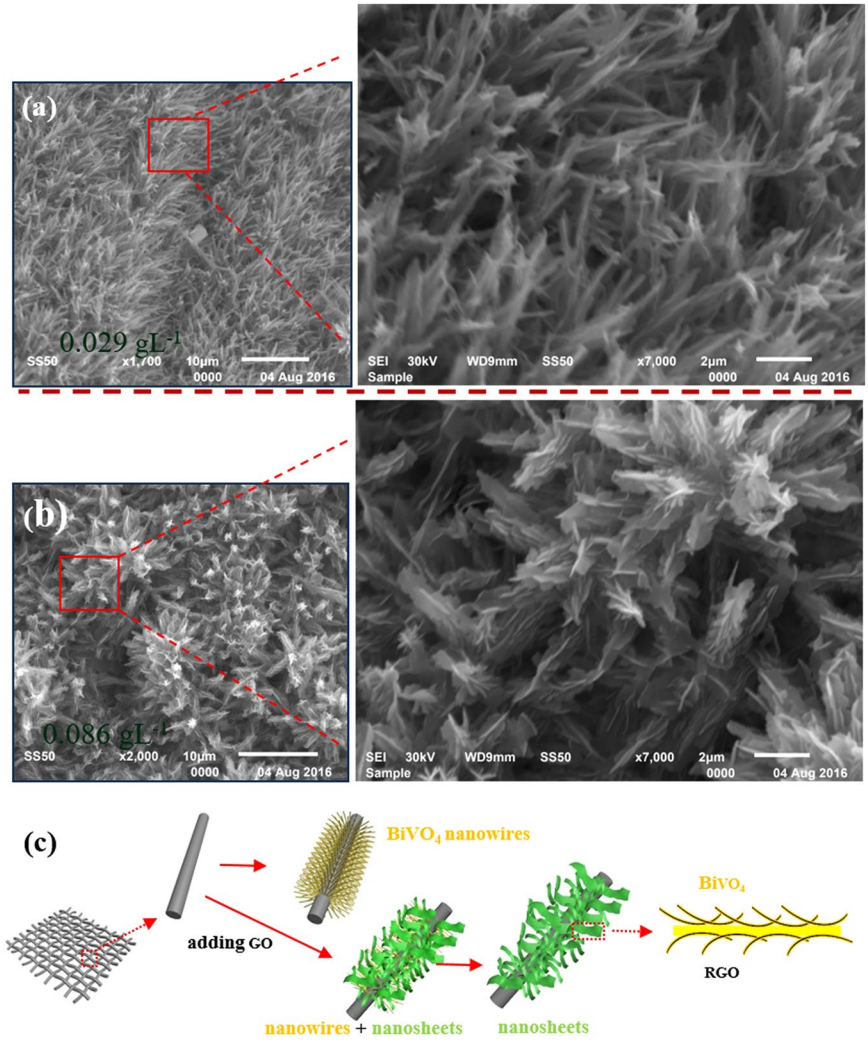

Figure 3. (**a**) and (**b**) SEM images of $BiVO_4$-0.029 and $BiVO_4$-0.086; (**c**) schematic illustration of the synthesis procedure of the $BiVO_4$ nanowires and $BiVO_4$-rGO nanosheets.

The normalized temporal concentration changes (C/C_0) of MO during the photocatalytic process are proportional to the normalized maximum absorbance (A/A_0), which can be derived from the change of the MO absorption profile at a given time interval. Figure 5a shows that the adsorption-desorption equilibrium attained in 210 minutes and the adsorption capacity were 7.30% and 5.10% of the MO for $BiVO_4$-rGO nanocomposite arrays (black) and the $BiVO_4$ nanowire arrays (red), respectively. As can be seen in Fig. 5b, the degradation of the MO solution exhibited a small decrease without the photocatalyst under visible-light irradiation, this decrease was 9.4% for 150 min of irradiation, indicating that the MO was stable. The photocatalytic performance of the $BiVO_4$-rGO composites is dependent on the proportion of rGO in the composite. Under simulated sunlight irradiation for 150 min, pure rGO and $BiVO_4$ exhibit 59.50% and 57.55% degradation efficiency for MO, respectively. When rGO is introduced into $BiVO_4$, the removal rate is increased to 85.03% for $BiVO_4$-0.029, and reaches a maximum value of 98.95% for $BiVO_4$-0.057, while the removal rate is 89.37% and 88% for $BiVO_4$-0.086 and $BiVO_4$-0.114, respectively. The $BiVO_4$-rGO composites exhibit a slightly lower activity, which is still significantly higher than that of the pure $BiVO_4$ sample. It is known that during photocatalysis, the light absorption and the charge transportation and separation are crucial factors; these energy levels are beneficial for the transfer of photo-induced electrons from the $BiVO_4$ conduction band to the rGO, which can efficiently separate the photo-induced electrons efficiently and hinder the charge recombination in the electron-transfer processes[56], thus enhancing the photocatalytic performance. However, when the rGO content is further increased above its optimum value, the photocatalytic performance deteriorates. This is ascribed to the following reasons: (i) rGO may absorb some visible light and thus cause a light harvesting competition between $BiVO_4$ and rGO with the increase of the rGO content, which leads to the decrease in the photocatalytic performance[57,58]; (ii) the excessive rGO can act as a kind of recombination center instead of providing an electron pathway and promoting the recombination of electron-hole pairs in the rGO[59].

UV-vis spectra are used to characterize the optical properties of the samples (Fig. 6a). According to the spectra, all the samples express absorbance in the visible regions. The pure $BiVO_4$ exhibits an absorption edge at

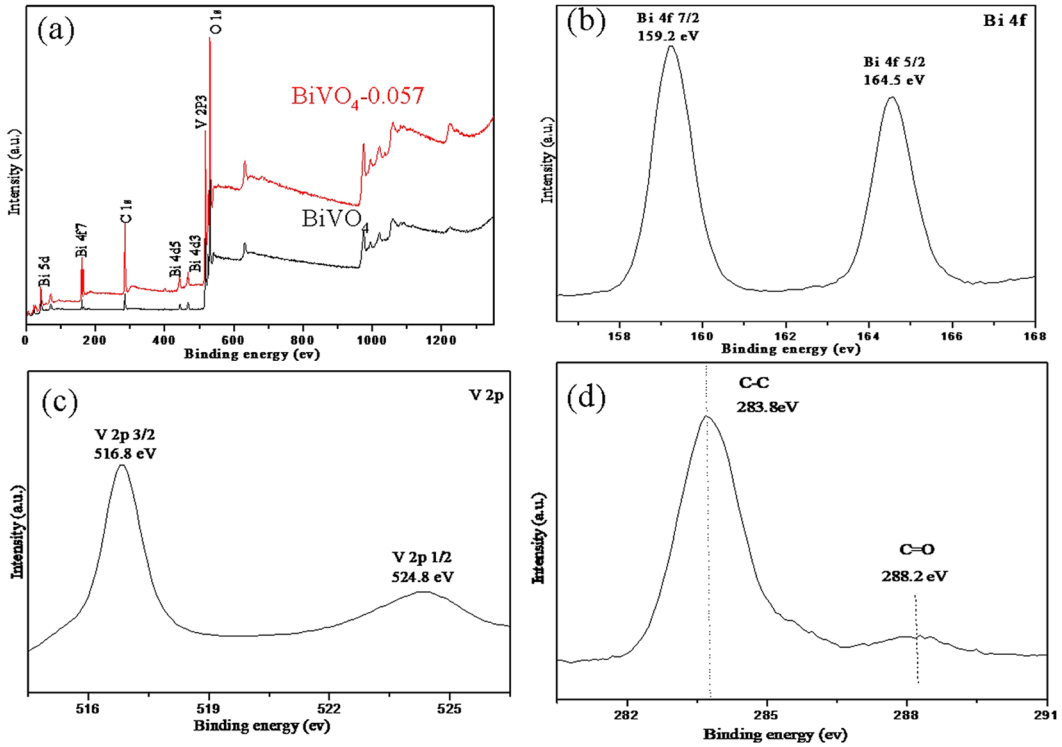

Figure 4. (**a**) Survey XPS spectra for $BiVO_4$ and $BiVO_4$-0.057, (**b**) Bi 4 f, (**c**) V 2p and (**d**) C 1 s for $BiVO_4$-0.057.

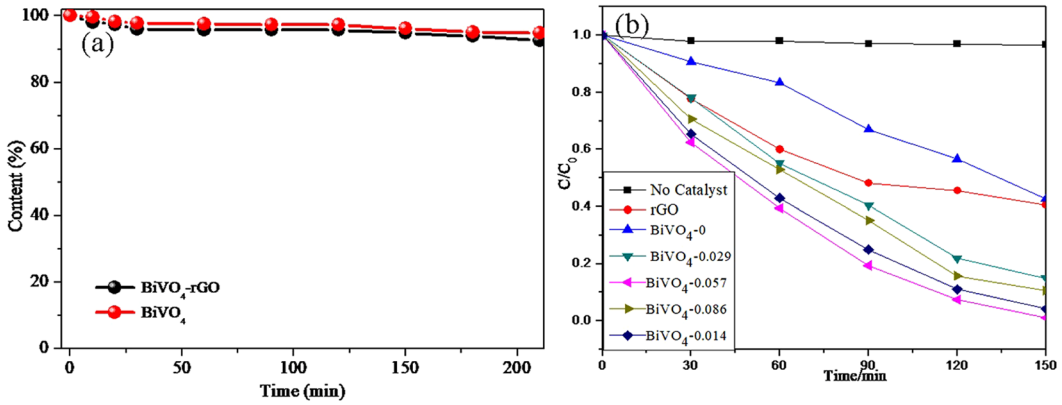

Figure 5. (**a**) The adsorption removal of MO in the dark by $BiVO_4$-rGO nanocomposite arrays (black) and $BiVO_4$ nanowire arrays (red), (**b**) Time-online photocatalytic performance of $BiVO_4$ and $BiVO_4$-rGO nanocomposite photocatalysts with different concentration of GO for the degradation of MO under simulated sunlight.

around 515.41 nm, showing a good visible light response. Accompanied by the introduction of rGO, the obtained $BiVO_4$-0.057 composite exhibits an absorption edge at around 529.48 nm and a broader visible light absorption in the range of 500–700 nm. These results further confirm that the existence of rGO in the $BiVO_4$-rGO composite greatly improves the visible-light absorption properties of the composite. Furthermore, the optical bandgap energy (Eg) of the obtained samples can be estimated from the formula $(\alpha h\nu) = A(h\nu\text{-}Eg)^{n/2}$ [60,61], where α is the absorption coefficient, h is Planck's constant, A is a constant, ν is the light frequency, and n = 1 and 4 for direct and indirect band gap materials, respectively. The optical transition of $BiVO_4$ is direct and the value of n is thus 1. As shown in Fig. 6b, the approximated band gaps of pure $BiVO_4$ and $BiVO_4$-0.057 are 2.41 and 2.34 eV, respectively. The narrowing of the band gap can be ascribed to the chemical bonding between $BiVO_4$ and the specific sites of GO during the hydrothermal treatment. This indicates that the $BiVO_4$-rGO nanocomposites can be photoexcited to generate more electron-hole pairs under visible-light irradiation, which can result in a higher photocatalytic performance.

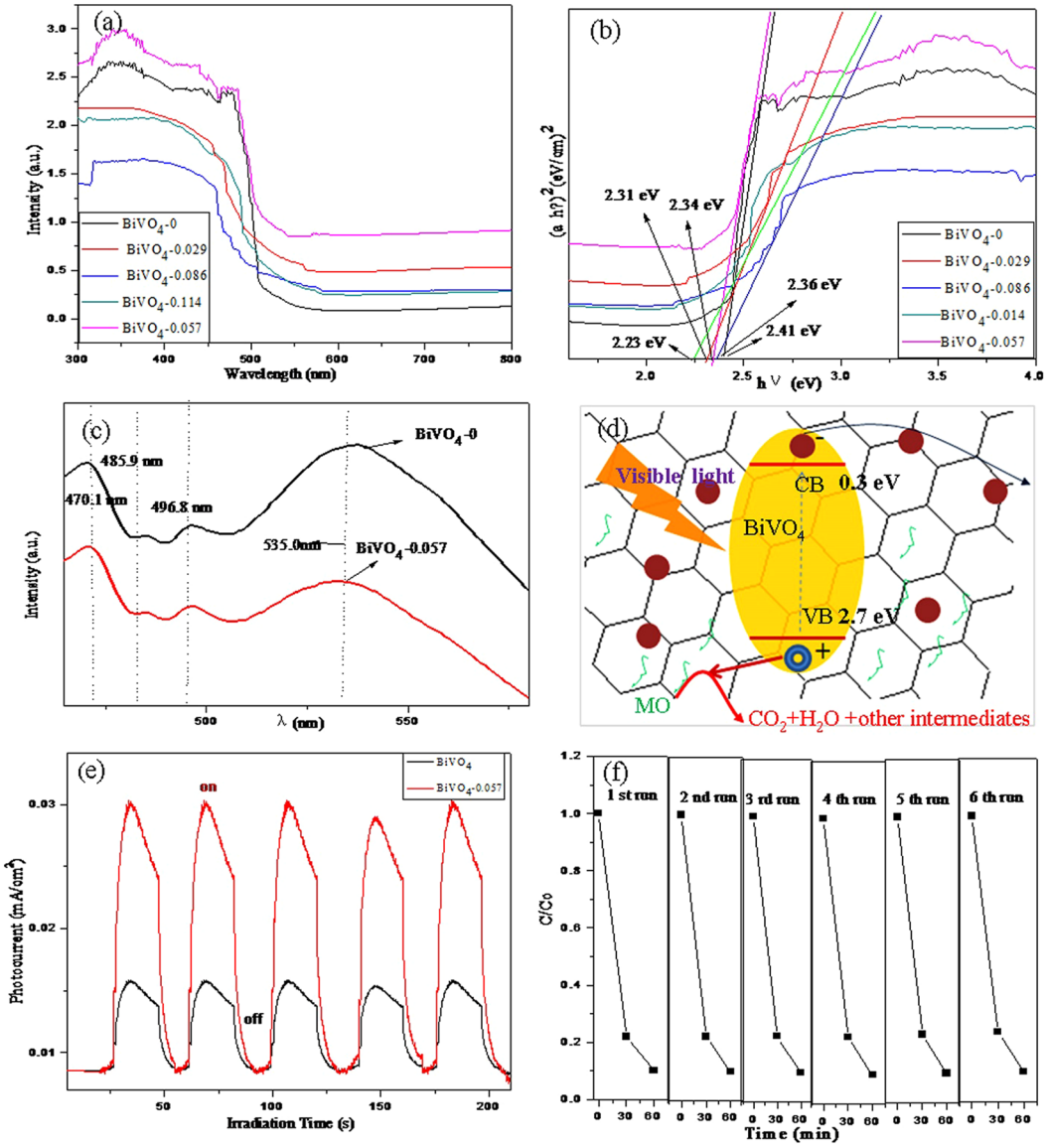

Figure 6. (**a**) and (**c**) UV-vis diffuse reflectance and photoluminescence spectral of bare $BiVO_4$ and $BiVO_4$-rGO nanocomposites, (**b**) plots of $(\alpha h\nu)^2$ versus photon energy ($h\nu$) of $BiVO_4$ and $BiVO_4$-0.057 nanocomposites, (**d**) schematic diagram for illuminating the charge behavior at the interface of $BiVO_4$ and rGO, (**e**) Photocurrent densities of bare $BiVO_4$ nanowire arrays (black) and $BiVO_4$-rGO nanocomposite (red) under simulated sunlight, (**f**) 6 cycles of the photocatalytic degradation of MO using $BiVO_4$-rGO as the photocatalyst under visible-light irradiation for 60 min.

In addition, the photoluminescence (PL) spectrum is regarded as a significant emission signal of carrier recombination. The transfer property of the photogenerated carriers (electron-hole pairs) can be evaluated by this method. Usually, a weaker PL intensity indicates a stronger ability for the separation of photo-generated carriers[62]. Figure 6c shows the PL emission spectra of pure $BiVO_4$ and the $BiVO_4$-0.057 photocatalysts monitored at an excitation wavelength of 320 nm. The peak at ~535 nm corresponds to the recombination of the hole formed in the O 2p band and the electron in the V 3d band[63], corresponding to the near band edge emission (NBE) of $BiVO_4$[64]. A decrease in PL intensity is clearly evident for the $BiVO_4$-0.057 due to the effective separation of electron-hole pairs. The photo-generated electrons in the excited $BiVO_4$ are transferred to the rGO nanosheets immediately after the photo-production, separating the photo-generated electrons and holes and inhibiting their recombination (Fig. 6d). This may be the reason that the $BiVO_4$-rGO sample exhibits an enhanced photocatalytic efficiency under visible light irradiation.

Figure 6e illustrates the photocurrent responses of the $BiVO_4$-rGO as photoelectrode under intermittent illumination by simulated sunlight and compared with that of the bare $BiVO_4$ nanowire arrays. The photocurrent density is much higher for the $BiVO_4$-rGO nanocomposite arrays than for the $BiVO_4$ nanowire arrays, suggesting that the charge carriers that are photogenerated for the $BiVO_4$-rGO persist than those for the $BiVO_4$ nanowire

arrays. This is not surprising because the photo-responsive rGO contributes to the photocurrent. Further, the rGO possesses an enhanced charge mobility compared with the $BiVO_4$ nanowire arrays.

Figure 6f shows the results of five successive runs for the photo-degradation of MO for the $BiVO_4$-rGO composite photocatalyst under the same experimental conditions. There is no apparent loss of photoactivity after six consecutive photo-degradation cycles. Therefore, the $BiVO_4$-rGO composites possess excellent stability and are not prone to be suffer from photo-corrosion during the degradation process.

Conclusions

In summary, a novel $BiVO_4$-rGO photocatalyst was successfully synthesized via a simple one-step hydrothermal method. Based on the narrow band gap (2.34 eV) and the relatively low PL intensity, the added rGO can effectively suppress the complex of light-generated electron-hole and increase the separation efficiency of photon-generated carrier, thereby enhancing the catalytic activity of the composite photocatalyst. The synthesized composite photocatalysts showed much higher photocatalytic activity than that of pure $BiVO_4$ with regarding to MO degradation under visible light. The present recoverable $BiVO_4$-rGO composite photocatalysts can be regards as one of the ideal photocatalysts for the various potential applications.

Experimental Section

Synthesis of a uniform $BiVO_4$ nanowires. All reagents were of analytical grade and used as received without further purification. In a typical procedure, NH_4VO_3, oxalic acid, hexamethylenetetramine and Bi $(NO_3)_3$ $5H_2O$ (the molar ratio 30:60:6:1) were dissolved into deionized water under ultrasonication for 1 h at room temperature. The dark blue mixture solution and a piece of pretreated Ti fabric, which has been rinsed with pure ethanol and deionized water for 1 h, were transferred into an autoclave, and then kept at 150 °C for 1 h in an oven. Finally, after cooling to room temperature, the Ti fabric with the as-prepared samples was rinsed with deionized water and dried at 80 °C for 12 h.

Synthesis of a $BiVO_4$-rGO nanocomposite photocatalysts. First of all, graphene oxide (GO) was prepared by a modified Hummer's method[30], graphene oxide (0.057 g) was sonicated in 100 mL water for 10 min. The nanocomposites were prepared by mixing the prepared graphene oxide suspension into the solution with NH_4VO_3, oxalic acid, hexamethylenetetramine and Bi $(NO_3)_3$ $5H_2O$ (the molar ratio 30:60:6:1), which was followed by vigorous magnetic stirring at room temperature for 1 h. Finally, the resulting mixture and a piece of pretreated Ti foil were then transferred to an autoclave and kept at 150 °C for 1 h. The final products were collected by centrifugation, and washed with deionized water and ethanol for three times, before drying at 80 °C for 12 h. The $BiVO_4$-rGO nanocomposites obtained by annealing the as-prepared samples attached to the Ti foil substrate at 200 °C in nitrogen for 2 h with a heating rate of 1 °C min^{-1}. To investigate the effect of GO concentration on the formation of $BiVO_4$-rGO nanocomposites, GO solutions with different concentrations (0, 0.029, 0.057, 0.086 and 0.114 gL^{-1}) were used in the same procedure, and are referred to as $BiVO_4$-0, $BiVO_4$-0.029, $BiVO_4$-0.057, $BiVO_4$-0.086 and $BiVO_4$-0.114, respectively, while keeping other conditions unchanged.

Photocatalytic Activity Measurements. Photocatalytic activities of the samples were evaluated by the degradation of methyl orange (MO) solution under simulated sunlight ($\lambda \geq 420$ nm) in a homemade reactor with a cooling water circulator assembled to keep the reactor at a constant temperature. Experiments were performed at ambient temperature as follows: $BiVO_4$ or $BiVO_4$-rGO nanocomposites (2 cm × 2 cm) grown on Ti fabric catalyst was added into 50 mL of 10 mg/L methyl orange (MO) solution. Before illumination, the solution was stirred for 30 min in the dark in order to reach the adsorption-desorption equilibrium for MO and dissolved oxygen. A 300 W xenon lamp with a 420 nm cutoff filter to remove any irradiation below 420 nm was used as the visible light source to trigger the photocatalytic reaction. The concentrations of the MO were monitored using a UV-2003 UV-vis spectrophotometer by checking the absorbance at 464 nm during the photodegradation process. A sample in approximately 2 mL was taken at the designed time interval during irradiation for chromatographic analysis.

The photocurrent measurements had been taken on a electrochemical working station (CHI-660C, China). The active area of the specimen was 2 × 2 cm^2 and the supporting electrolyte was 0.25 M Na_2SO_4 aqueous solution. A 300 W Xe-lamp was used to provide the simulated sunlight.

Characterization. The samples were characterized with X-ray diffraction (XRD; Bruker D8 X-ray diffractometer). The morphology of the sample was investigated by a field-emission scanning electron microscope (FE-SEM; Hitachi S-4800) and a transmission electron microscope (TEM; JEOL-2100F at 200 kV). Energy Dispersive Spectroscopy (EDS) were used to determine morphology and elemental composition of the sample in the TEM. Raman spectra of GO, $BiVO_4$, and $BiVO_4$-rGO were recorded using a Raman spectroscope (JY-HR800, the excitation wavelength of 633 nm). UV-vis diffuse reflectance spectra (DRS) of the as-prepared samples were obtained using a Shimadzu UV-2550 spectrophotometer equipped with an integrating sphere using $BaSO_4$ as the reflectance standard. The chemical composition of the sample was analyzed by X-ray photoelectron spectroscopy (XPS) using KAlpha 1063 (Thermo Fisher Scientific, UK). The photoluminescence (PL) spectral measurements were carried out on a Hitachi F-2500 fluorescence spectrophotometer with a Xe lamp as the light source.

References

1. Hisaindee, S. *et al.* Application of LC-MS to the analysis of advanced oxidation process (AOP) degradation of dye products and reaction mechanisms. *Trends. Anal. Chem.* **49**, 31–44 (2013).
2. Rauf, M. A. *et al*. Adsorption of dyes from aqueous solutions onto sand and their kinetic behavior. *Chem. Eng. J.* **137**, 238–243 (2008).
3. Jamal, F. *et al.* Biocatalytic activity of immobilized pointed gourd (Trichosanthes dioica) peroxidase-concanavalin A complex on calcium alginate pectin gel. *J. Mol. Catal. B. Enzym.* **74**, 125–131 (2012).

4. Tsantaki, E. T. *et al*. Anodic oxidation of textile dyehouse effluents on boron-doped diamond electrode. *J. Hazard. Mater.* **207**, 91–96 (2012).
5. Hou, M. F. *et al*. Degradation of rhodamine B by Fe(0)-based Fenton process with H_2O_2. *Chemosphere.* **83**, 1279–1283 (2011).
6. Mozia, S. *et al*. Photocatalytic degradation of azo-dye Acid Red 18. *Desalination.* **185**, 449–456 (2005).
7. Silva, C. G. *et al*. Photocatalytic and photochemical degradation of mono-, di- and tri-azo dyes in aqueous solution under UV irradiation. *J. Photochem. Photobiol. A.* **181**, 314–324 (2006).
8. Liang, Y. *et al*. Oil-in-water self-assembled Ag@AgCl QDs sensitized Bi_2WO_6: Enhanced photocatalytic degradation under visible light irradiation. *Appl. Catal. B. Environ.* **164**, 192–203 (2015).
9. Chen, Z. *et al*. Enhanced photocatalytic performance over $Bi_4Ti_3O_{12}$, nanosheets with controllable size and exposed {0 0 1} facets for Rhodamine B degradation. *Appl. Catal. B. Environ.* **180**, 698–706 (2016).
10. Wang, H. *et al*. Enriched photoelectrocatalytic degradation and photoelectric performance of BiOI photoelectrode by coupling rGO. *Appl. Catal. B. Environ.* **208**, 22–34 (2017).
11. Li, Y. *et al*. Removal of Cr(VI) by 3D TiO_2-graphene hydrogel via adsorption enriched with photocatalytic reduction. *Appl. Catal. B. Environ.* **199**, 412–423 (2016).
12. Liu, L. *et al*. A stable Ag_3PO_4 @PANI core@shell hybrid: enrichment photocatalytic degradation with π-π conjugation. *Appl. Catal. B. Environ* **201**, 92–104 (2016).
13. Li, L. *et al*. A stable Ag_3PO_4 @g-C_3N_4, hybrid core@shell composite with enhanced visible light photocatalytic degradation. *Appl. Catal. B. Environ* **183**, 133–141 (2015).
14. Zhou, L. *et al*. A sonochemical route to visible-light-driven high-activity $BiVO_4$ photocatalyst. *J. Mol. Catal. A. Chem.* **252**, 120–124 (2006).
15. Huang, Z. F. *et al*. Nanostructured bismuth vanadate-based materials for solar-energy-driven water oxidation: a review on recent progress. *Nanoscale.* **6**, 14044–14063 (2014).
16. Wang, W. W. *et al*. ZnO-SnO_2, Hollow Spheres and Hierarchical Nanosheets: Hydrothermal Preparation, Formation Mechanism, and Photocatalytic Properties. *Adv. Funct. Mater.* **17**, 59–64 (2007).
17. Zhang, L. *et al*. Controllable synthesis of Bi_2MoO_6, and effect of morphology and variation in local structure on photocatalytic activities. *Appl. Catal. B. Environ.* **98**, 138–146 (2010).
18. Yang, M. *et al*. Facile microwave-assisted synthesis and effective photocatalytic hydrogen generation of Zn_2GeO_4 with different morphology. *RSC Adv.* **4**, 15048–15054 (2014).
19. Li, G. *et al*. Difference in valence band top of $BiVO_4$ with different crystal structure. *Mater. Chem. Phys.* **136**, 930–934 (2012).
20. Kohtani, S. *et al*. Loading effects of silver oxides upon generation of reactive oxygen species in semiconductor photocatalysis. *Phys. Chem. Chem. Phys.* **10**, 2986–2992 (2008).
21. Yan, Y. *et al*. Microwave-assisted *in situ* synthesis of reduced graphene oxide-$BiVO_4$ composite photocatalysts and their enhanced photocatalytic performance for the degradation of ciprofloxacin. *J. Hazard. Mater.* **250**, 106–114 (2013).
22. Jiang, H. *et al*. Fabrication and efficient photocatalytic degradation of methylene blue over CuO/$BiVO_4$, composite under visible-light irradiation. *Mater. Res. Bull.* **44**, 700–706 (2009).
23. Wang, Y. *et al*. Microwave synthesis and photocatalytic activity of Tb(3+) doped $BiVO_4$ microcrystals. *J. Colloid. Interf. Sci.* **483**, 307–313 (2016).
24. Li, J. *et al*. Controlled synthesis of $BiVO_4$/$SrTiO_3$ composite with enhanced sunlight-driven photofunctions for sulfamethoxazole removal. *J. Colloid. Interf. Sci.* **485**, 116–122 (2016).
25. Joaquin, R. *et al*. TiO_2/$BiVO_4$ Nanowire Heterostructure Photoanodes Based on Type II Band Alignment. *ACS. Cent. Sci.* **2**, 80–88 (2016).
26. Zhao, J. *et al*. High-Performance Ultrathin $BiVO_4$ Photoanode on Textured Polydimethylsiloxane Substrates for Solar Water Splitting. *ACS. Energy. Lett.* **1**, 68–75 (2016).
27. Kong, H. J. *et al*. Sulfur-Doped g-C_3N_4/$BiVO_4$ Composite Photocatalyst for Water Oxidation under Visible Light. *Chem. Mater.* **28**, 1318–1324 (2016).
28. Balachandran, S. *et al*. The simple, template free synthesis of a Bi_2S_3-ZnO heterostructure and its superior photocatalytic activity under UV-A light. *Dalton Trans.* **42**, 5338–5347 (2013).
29. Gao, X. *et al*. Formation of Mesoporous Heterostructured $BiVO_4$/Bi_2S_3 Hollow Discoids with Enhanced Photoactivity. *Angew. Chem. Int. Ed.* **53**, 5917–21 (2014).
30. Zhou, D. *et al*. Solvothermal synthesis and characterization of a novel reduced graphene oxide (RGO)/$BiVO_4$/SiO_2, nanocomposites. *Mater. Lett.* **185**, 32–35 (2016).
31. Mao, M. *et al*. Facile synthesis of porous Bi_2O_3-$BiVO_4$ p-n heterojunction composite microrods with highly efficient photocatalytic degradation of phenol. *J. Alloys Compd* **688**, 1080–1087 (2016).
32. Lin, Z. *et al*. A sonochemical route to visible-light-driven high-activity $BiVO_4$, photocatalyst. *J. Mol. Catal. A. Chem.* **252**, 120–124 (2006).
33. Pan, X. *et al*. Morphology control, defect engineering and photoactivity tuning of ZnO crystals by graphene oxide–a unique 2D macromolecular surfactant. *Phys. Chem. Chem. Phys.* **16**, 5589–5599 (2014).
34. Zhang, N. *et al*. Waltzing with the Versatile Platform of Graphene to Synthesize Composite Photocatalysts. *Chem.Rev.* **115**, 10307–10377 (2015).
35. Han, C. *et al*. Structural diversity of graphene materials and their multifarious roles in heterogeneous photocatalysis. *Nano Today.* **11**, 351–372 (2016).
36. Zhang, Y. *et al*. TiO_2-Graphene Nanocomposites for Gas-Phase Photocatalytic Degradation of Volatile Aromatic Pollutant: Is TiO_2-Graphene Truly Different from Other TiO_2-Carbon Composite Materials. *Acs Nano.* **4**, 7303–7311 (2010).
37. Yang, M. Q. *et al*. Metal-free, robust, and regenerable 3D grapheme-organics aerogel with high and stable photosensitization efficiency. *Journal of Catalysis.* **346**, 21–29 (2017).
38. Yu, J. *et al*. Effects of Structural Variation on the Photocatalytic Performance of Hydrothermally Synthesized $BiVO_4$. *Adv. Funct. Mater.* **16**, 2163–2169 (2006).
39. Zhang, A. P. *et al*. Effects of pH on Hydrothermal Synthesis and Characterization of Visible-light-driven $BiVO_4$ Photocatalyst. *J. Mol. Catal. A. Chem.* **304**, 28–32 (2009).
40. Zou, Y. Q. *et al*. NiO nanosheets grown on graphene nanosheets as superior anode materials for Li-ion batteries. *Nanoscale.* **3**, 2615–2620 (2011).
41. Zhao, K. *et al*. Long Cycling Life Supercapacitors Electrode Materials: Ultrathin Manganese Dioxide Nanoscrolls Adhered to Graphene by Electrostatic Self-Assembly. *Electrochimica Acta* **174**, 1234–1243 (2015).
42. Sang, Y. *et al*. Enhanced photocatalytic property of reduced graphene oxide/TiO_2 nanobelt surface heterostructures constructed by an *in situ* photochemical reduction method. *Small.* **10**, 3775–3782 (2014).
43. Li, J. *et al*. Facile synthesis and high activity of novel $BiVO_4$/$FeVO_4$, heterojunction photocatalyst for degradation of metronidazole. *Appl. Surf. Sci.* **351**, 270–279 (2015).
44. Hu, W. H. *et al*. MoSx supported graphene oxides with different degree of oxidation as efficient electrocatalysts for hydrogen evolution. *Carbon.* **100**, 236–242 (2016).
45. Wang, Y. *et al*. Electrostatic self-assembly of $BiVO_4$-reduced graphene oxide nanocomposites for highly efficient visible light photocatalytic activities. *ACS Appl. Mater. Interfaces.* **6**, 12698–12706 (2014).

46. Yun, H. N. *et al*. Reducing Graphene Oxide on a Visible-Light $BiVO_4$ Photocatalyst for an Enhanced Photoelectrochemical Water Splitting. *J. Phys. Chem. Lett.* **1**, 2607–2612 (2010).
47. Li, H. P. *et al*. Synthesis and characterization of g-C_3N_4/Bi_2MoO_6 heterojunctions with enhanced visible light photocatalytic activity. *Appl. Catal. B Environ.* **161**, 89–97 (2014).
48. Chen, L. *et al*. Porous peanut-like Bi_2O_3-$BiVO_4$ composites with heterojunctions: one-step synthesis and their photocatalytic properties. *Dalton Trans.* **41**, 9513–9518 (2012).
49. He, Z. *et al*. BiOCl/$BiVO_4$ p–n heterojunction with enhanced photocatalytic activity under visible-light irradiation. *J. Phys. Chem. C.* **118**, 389–398 (2014).
50. Li, H. Q. *et al*. High photocatalytic performance of BiOI/Bi_2WO_6 toward toluene and Reactive Brilliant Red. *Appl. Surf. Sci.* **264**, 581–588 (2013).
51. Gui, M. S. *et al*. Preparation and visible light photocatalytic activity of Bi_2O_3/Bi_2WO_6, heterojunction photocatalysts. *J. Solid State Chem.* **184**, 1977–1982 (2011).
52. Ji, K. M. *et al*. Fabrication and high photocatalytic performance of noble metal nanoparticles supported on 3DOM $InVO_4$-$BiVO_4$, for the visible-light-driven degradation of rhodamine B and methylene blue. *Appl. Catal. B Environ.* **165**, 285–295 (2015).
53. Kang, Z. *et al*. Carbon dots and $BiVO_4$ quantum dots composites for overall water splitting via two-electron pathway. *Nanoscale.* **8**, 17314–17321 (2016).
54. Chen, F. *et al*. Hierarchical assembly of graphene-bridged Ag_3PO_4/Ag/$BiVO_4$, (040) Z-scheme photocatalyst: An efficient, sustainable and heterogeneous catalyst with enhanced visible-light photoactivity towards tetracycline degradation under visible light irradiation. *Appl. Catal. B-Environ.* **200**, 330–342 (2017).
55. Wang, P. *et al*. ZnO nanosheets/graphene oxide nanocomposites for highly effective acetone vapor detection. *Sensor. Actuat. B-Chem.* **230**, 477–484 (2016).
56. Guo, C. X. *et al*. Layered Graphene/Quantum Dots for Photovoltaic Devices. *Angew. Chem. Int. Ed.* **49**, 3014–3017 (2010).
57. Zhu, G. *et al*. Graphene-incorporated nanocrystalline TiO_2, films for CdS quantum dot-sensitized solar cells. *J. Electroanal. Chem.* **650**, 248–251 (2011).
58. Tang, Y. B. *et al*. Incorporation of Graphenes in Nanostructured TiO_2 Films via Molecular Grafting for Dye-Sensitized Solar Cell Application. *ACS Nano.* **4**, 3482–3488 (2010).
59. Yang, N. L. *et al*. Two-Dimensional Graphene Bridges Enhanced Photoinduced Charge Transport in Dye-Sensitized Solar Cells. *ACS Nano.* **4**, 887–894 (2010).
60. Shang, M. *et al*. A novel $BiVO_4$ hierarchical nanostructure: Controllable synthesis, growth mechanism, and application in photocatalysis. *Crystengcomm.* **12**, 1754–1758 (2010).
61. Zhang, L. S. *et al*. Fabrication of flower-like Bi_2WO_6 superstructures as high performance visible-light driven photocatalysts. *J. Mater. Chem.* **17**, 2526–2532 (2007).
62. Liu, Y. *et al*. Hydrothermal synthesis of hierarchical flower-like Bi_2WO_6, microspheres with enhanced visible-light photoactivity. *Mater. Lett.* **157**, 158–162 (2015).
63. Chen, L. *et al*. Hollow peanut-like m-$BiVO_4$: facile synthesis and solar-light-induced photocatalytic property. *CrystEngComm.* **14**, 4217–4222 (2012).
64. Karunakaran, C. *et al*. Electrical, optical and visible light-photocatalytic properties of monoclinic $BiVO_4$, nanoparticles synthesized hydrothermally at different pH. *Mater. Sci. Semicond. Process.* **21**, 122–131 (2014).

Acknowledgements

This work was supported by the Natural Science Foundation of China (Nos. 51201117,51503158), the Natural Science Foundation of Hubei Provience (No. 2015CFA123), Educational Commission of Hubei Province of China (No. 151086), The Natinal Key Research and Development Program of China (No.2016YFA0101102).

Author Contributions

D.F. designed experiments; X.J.L. carried out experiments; H.L., W.L.X., M.J., X.F., W.B.L. analyzed the data; D.F. drew the Figs 3(c) and 6(d); X.J.L. and D.F. wrote the manuscript.

Additional Information

Competing Interests: The authors declare that they have no competing interests.

Publisher's note: Springer Nature remains neutral with regard to jurisdictional claims in published maps and institutional affiliations.